ACI STRUCTURAL JOURNAL TECHNICAL PAPER

Title No. 119-S126

Reinforced Masonry Building under Lateral Loading—Numerical Study

by Sarkar Noor-E-Khuda

Fully grouted reinforced masonry (FGRM) walls, being an assemblage of hollow blocks with all cores grouted and vertical and horizontal reinforcements, offer unparalleled resistance to lateral and gravitational loading over their unreinforced counterparts. The Australian masonry standard AS 3700:2018 provides guidelines for the design of reinforced masonry walls to seismic or cyclonic loading with a minimum vertical and horizontal reinforcement ratio as low as 0.13% and 0.07%, respectively. The performance of FGRM shear walls in a building structure designed within the AS 3700:2018 provisions with a low reinforcement ratio has hardly been addressed by researchers. This paper investigates the structural performance of a three-story prototype FGRM building under quasi-static lateral loading applied severally from different directions. The assessment is carried out exclusively using an explicit finite element (EFE) model. The EFE model is briefly presented and the structural performance—that is, load capacity, stiffness, and displacement ductility—of the FGRM building and the component walls are discussed in detail. The structural performance of the walls of the prototype building is compared with similar walls (which were analyzed separately), and this comparison provides key insights on the influence of realistic end support conditions on the structural behavior of FGRM walls. It was found that the component walls of the prototype FGRM building experienced pure in-plane and out-of-plane loading, and their load-displacement relationship and failure pattern altered due to changes in the loading direction.

Keywords: explicit finite element (EFE) modeling; fully grouted (FG); lateral loading; reinforced masonry (RM); reinforcement.

INTRODUCTION

To enhance the axial and lateral load capacity, masonry walls constructed using hollow blocks are grouted and reinforced both vertically and horizontally, which are commonly referred to as reinforced masonry (RM) walls. RM walls are predominantly classified as fully grouted (FG) or partially grouted (PG), depending on the extent of grouting, and/or close- or wide-spaced, depending on the reinforcement detailing. The Australian masonry standard AS 3700:2018[1] defines RM walls as those containing main reinforcements in the form of vertical and horizontal reinforcements with a minimum reinforcement ratio of 0.13% and 0.07%, respectively, and a maximum spacing of 2000 and 3000 mm, respectively. AS 3700 also specifies the use of a minimum of 100 mm^2 of vertical reinforcement within 300 mm from the edges of the wall. Each reinforcing bar in the grouted cores (also referred to as "cells") is, according to AS 3700, to be surrounded by an annulus of grout of thickness twice the diameter of the reinforcing bar to prevent the bar from buckling under vertical compression loading. The standard also specifies the main reinforcements to be symmetrically positioned in the grouted cores, and adequately anchored and detailed using the design guidelines of the Australian concrete design standard AS 3600:2018.[2] One of the key aspects of the AS 3700 design standard is the use of a minimum reinforcement ratio (that is, 0.13% and 0.07% for vertical and horizontal reinforcement, respectively), which is comparatively lower[3] than the reinforcement ratio used in most of the experimental programs. For example, the vertical and horizontal reinforcement ratios used by Nolph and ElGawady[4] were 0.446% and 0.085%, respectively; Shing et al.[5] used 0.38 to 0.74% and 0.14 to 0.26%, respectively; Voon and Ingham[6] used 0.61% and 0.05 to 0.14%, respectively; and Shedid et al.[7] used 0.29 to 1.31% and 0.08 to 1.13%, respectively. AS 3700 outlines the FG system as those with all hollow cores grouted and the PG system as the ones where only the cores containing reinforcements are grouted. The structural performance of these systems—that is, load capacity and ductility—vary as per the structural configuration.[3] The FG system provides a regular grouted masonry section throughout the length and width of the wall, unlike the PG system, which contains weaker ungrouted pockets.[8] Recent research[9-11] confirms that the PG walls mostly experience cracking along the weaker unreinforced/ungrouted masonry portion and in-cases, without yielding the reinforcing bars. Therefore, an investigation is needed to evaluate the structural performance of fully grouted reinforced masonry (FGRM) walls in a building structure designed with low vertical and horizontal reinforcement content, and assess the contribution of those reinforcements in the lateral load-resisting mechanism. While a majority of structural investigations on the various RM systems covered the performance of individual walls,[6,10,12-18] the work presented in this paper examines the structural performance of a building.

During their service life, masonry walls experience vertical compression loading from the slabs/floors above,[19] and lateral in-plane and out-of-plane loading through the diaphragm action during seismic or cyclonic events. Hence, several experimental, analytical, and numerical assessments on RM walls were undertaken by researchers in the past. This paper recognizes the experimental[4,6,12,15,17,20-25] and finite

ACI Structural Journal, V. 119, No. 6, November 2022.
MS No. S-2021-109.R4, doi: 10.14359/51734794, received April 12, 2022, and reviewed under Institute publication policies.

element (FE)-based[14,26-33] research work on the in-plane and out-of-plane structural performance of masonry walls as found in the literature. It should be noted that loads induced by the vertical component of an earthquake ground motion and/or horizontal load from the impact of an intruding vehicle have not been considered in the analysis.

While several authors (including Dhanasekar and Haider,[14] Lourenço,[29] and Voon and Ingham[34]) coupled the effect of axial compression and lateral action in their assessments, the interaction of combined in-plane and out-of-plane loading caused due to the irregularities in the building floor plan is hardly addressed by researchers.[26,27] Furthermore, the behavior of the component walls in a building structure with practicable reinforcement detailing, end support arrangements, and under realistic loading conditions can be significantly different[35-37] than those of the individually analyzed walls, which triggers the need for the structural performance assessment of multi-story RM buildings. The presence of additional floors and spans in a multi-story structure has the potential to influence the structural response[38-45] and affect the performance of the component walls of the building, which is difficult to simulate on individually analyzed walls.

With recent advancements in computational facilities and the availability of sophisticated computer programs, the FE method offers an economical and appropriate alternate approach to the experimental counterpart. Bolhassani et al.[11] adopted a micro-FE model and assessed the structural performance of a one-span single-story partially grouted reinforced masonry (PGRM) building and showed a promising gain in load capacity and ductility from the detailed designed walls. However, the performance of the component walls, effect of multiple stories/spans, changes in the loading direction, and discussion on the failure modes were not addressed; consideration of these elements is necessary to assess the influence of the practicable loading and boundary conditions on the structural performance of buildings. This paper presents the detailed structural performance of a two-span and three-story FGRM prototype building subjected to quasi-static lateral loading. The prototype building adopted a structural design within the current AS 3700 code provisions, suitable for moderate earthquake loading. The assessment has been carried out using an explicit finite element (EFE) model, recently developed by the author. The EFE model incorporated macroscopic masonry properties and successfully simulated the out-of-plane,[28] in-plane,[10,14] and combined loading[27] performance of RM walls.

This paper briefly describes the EFE model and its application to a prototype building. A detailed assessment of the building and the component walls are presented. Outcomes from the EFE model are compared with those obtained from the prevailing Australian standards and the literature for further justification.

RESEARCH SIGNIFICANCE

The work presented in this paper is one of the rare studies on an entire building structure rather than the component walls only, which has been extensively investigated by researchers in the past. The reinforcement ratios used in this study are closer to the typical reinforcement ratios used in actual RM buildings.

THREE-STORY FGRM BUILDING

Details of the three-story prototype FGRM building including geometric, loading, and structural configurations are discussed in this section.

Geometry

The geometric and structural configurations of the prototype FGRM building, including the wall layout and the component wall details, are schematically illustrated in Fig. 1.

Design

The design of the prototype building and its desired response was directed primarily by the capacity design guidelines outlined in the AS 3700:2018 and AS 1170.4-2007[46] code provisions. The adopted design for the prototype building aimed to: 1) provide adequate strength; 2) provide an acceptable level of displacement ductility (minimum of 2.0 for RM structures as in Section 6.5 of AS 1170.4); and 3) sustain in seismic zones within hazard factor Z_{sit} of 0.3 (AS 1170.4), which covers the majority of metropolitan and regional Australia. As the load capacity of RM walls (as of AS 3700) increases with increasing design cross-sectional and reinforcing bar area, the FGRM system appears to be the most appropriate for multi-story construction in moderate seismic regions. In contrast, the ductility of the masonry system improves with the addition of reinforcement; however, there is no design equation available in AS 3700 to quantify the ductility of a wall in a process similar to the in-plane, out-of-plane, and compression capacity calculations. Furthermore, over-reinforcing a brittle system such as masonry can probably lead to brittle compression failure, which occurs explosively and without warning.[23] A limiting value of the reinforcement ratio for RM systems is thus essential to ensure the efficiency of the embedded reinforcement. As such, all the component walls were reinforced to fulfill the code requirements for minimal reinforcement. A vertical reinforcement ratio of 0.002 (0.0023 for walls CD, BE, AF) and a horizontal reinforcement ratio of 0.0008 was adopted in the structural design of the walls, which meets the AS 3700 requirements for minimum vertical and horizontal reinforcement of 0.0013 and 0.0007, respectively. The same reinforcement detailing (reinforcement spacing, reinforcing bar area) was followed in all the component walls (Fig. 1) considering its practicability and ease in construction. Each vertical and horizontal reinforced core contained one D16 and one D10 reinforcing bar, respectively. Both the vertical and the horizontal reinforcements were equally spaced at 600 mm center-to-center, except those next to the window/door openings. Reinforcement detailing of the walls is shown in Fig. 1(b) to (e). Vertical and horizontal reinforcing bars were provided within 100 mm from the structural end of the wall and next to the openings. The horizontal reinforcement bands located above the door and above and below the window openings contented the lintel bands, which provided sufficient stability to the walls. Because the

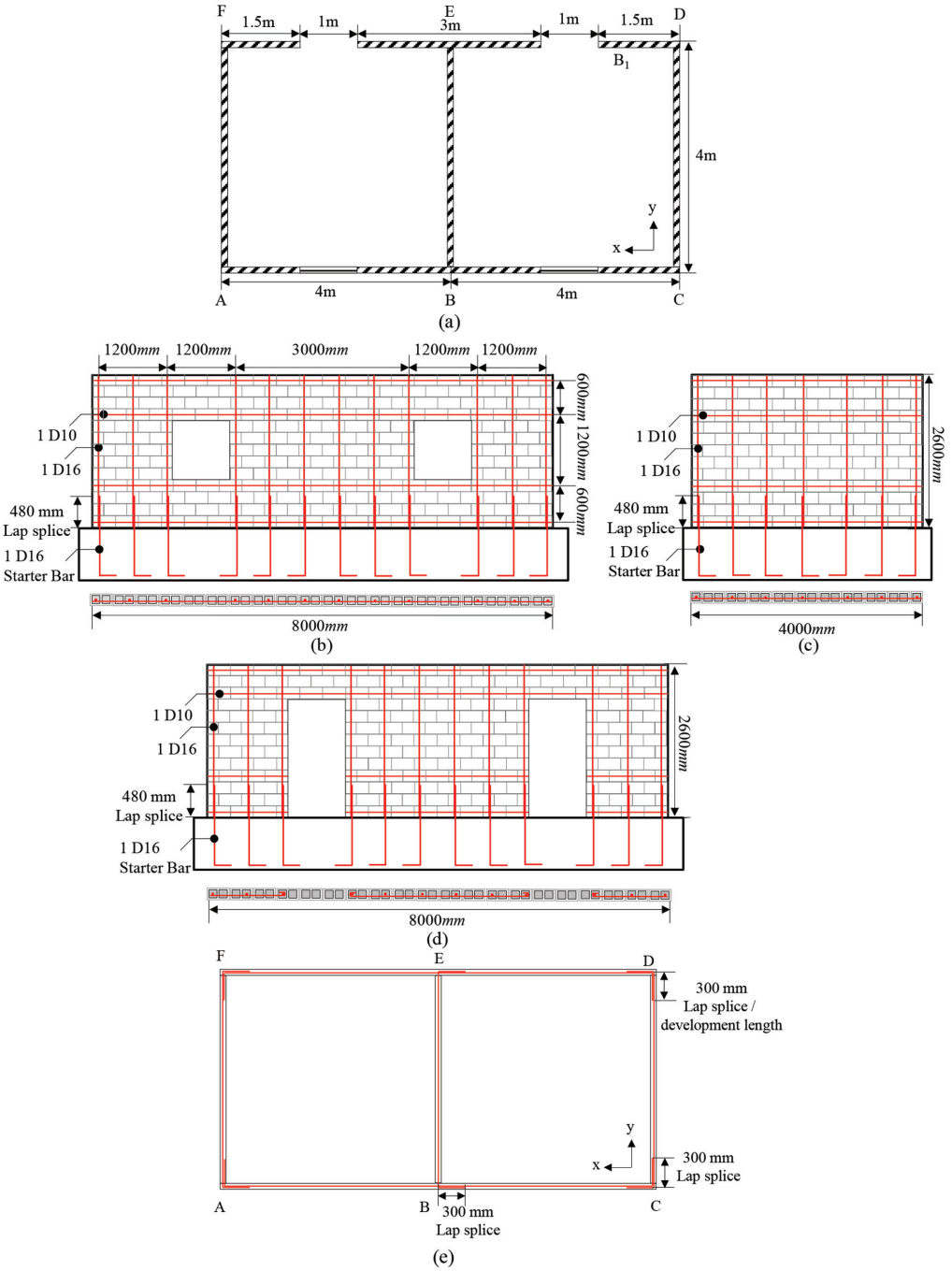

Fig. 1—Configuration of prototype FGRM building: (a) wall layout; (b) wall AC; (c) walls CD, BE, and AF; (d) wall DF; and (e) horizontal reinforcement lap-splice and connection detail.

interaction between the substructure and superstructure can influence the load distribution mechanism,[47] in the design, the vertical reinforcements of RM walls were considered connected to the foundation using starter bars embedded into the foundation slab (as shown in Fig. 1). This also ensured proper anchorage of the vertical reinforcements as specified in AS 3700. The starter bars were tied to the vertical reinforcements of the wall using steel ties as per the lap-splice design requirements of AS 3600. The horizontal reinforcements were designed to extend into the adjacent walls and/or connect to the horizontal reinforcements of the adjacent walls[20] and provide the required anchorage as specified in AS 3700 and AS 3600.

The building was designed as an ordinary residential dwelling considering structural importance level 2, a service life span of 50 years, and a live load of 4 kPa (AS 1170.4). In the FE model, the bottom edge of the ground-floor walls was assumed as fixed through a monolithic connection to the base slab—a common practice for RM walls. All the wall intersections were modeled as monolithic, which provided full moment resistance.

MODELING

The EFE model and its application in the analysis of the prototype FGRM building and its component walls are briefly discussed in this section.

Explicit finite element model

The EFE model recently developed by the author is adopted in this study.[28] The model uses a four-node, triple-layered shell element (S4R) with seven-point Simpson's integration for each layer. Both the exterior layers of the element representing the masonry face shells were assigned with unreinforced masonry material properties, while the intermediate layer representing the FG cores was assigned with the damaged plasticity material model for concrete. Reinforcement was distinctly modeled using the one-dimensional truss element (T3D2), which were tied to the nodes of the S4R element at the designated locations as per the adopted design detail shown in Fig. 1.

The macroscopic material model representing unreinforced masonry is defined using the multi-surface plasticity theory proposed by Lourenço.[29] The model contains tensile and compressive strength in directions parallel and normal to the bed joint, and the subsequent exponential tensile- and compression-softening parameters. The composite masonry material model requires four uniaxial strength parameters (f_{tp}, f_{tn}, f_{cp}, and f_{cn}) and four inelastic energy parameters (G_{ftp}, G_{ftn}, G_{fcp}, and G_{fcn}). In addition, parameters for shear stress contribution to tension failure (α), shear stress contribution to compression failure (γ), biaxial compressive strength (β), and equivalent plastic strain (κ_p) corresponding to the peak compressive strength were taken from the literature. The material model was incorporated into the Abaqus/Explicit program in a VUMAT subroutine; more details are reported in Noor-E-Khuda et al.[28,48] and Dhanasekar and Haider.[14]

The concrete damaged plasticity model[49] available in Abaqus was used to simulate the grout material. The failure mechanism of the grout, similar to concrete, was fundamentally defined by tensile cracking and compression crushing. Under compression, grout exhibits an elastic-plastic and post-peak softening response; under tension, it exhibits an elastic and post-peak softening response. In addition, parameters for dilation angle, the flow potential eccentricity, the ratio of initial equivalent biaxial compressive yield stress to initial uniaxial compressive yield stress, and the ratio of the second stress invariant on the tensile meridian to that on the compressive meridian for the grout material were defined.

The stress-strain relation for reinforcement was defined using an elastic-plastic material model incorporated in the VUMAT user material subroutine. The steel was assumed to yield in tension but remained elastic under compression. The elastic behavior of the vertical reinforcements at a low level of axial compression load (that is, 0.33 MPa) was also observed by Andolfato et al.[19] and Zahra et al.,[50] which further justifies the assumptions made in the material model.

The EFE model parameters were calibrated using the four-point bending test data set of a series of FGRM walls of size 1.22 m long x 2.64 m high x 0.15 m thick.[23] The walls consisted of two No. 5 (16 mm) bars as vertical reinforcements at 610 mm centers and four No. 3 (10 mm) bars as horizontal reinforcements at 810 mm centers at the mid-thickness. The adopted reinforcement detailing as well as the thickness and height of the wall of the prototype building is consistent with the validated EFE model. Details

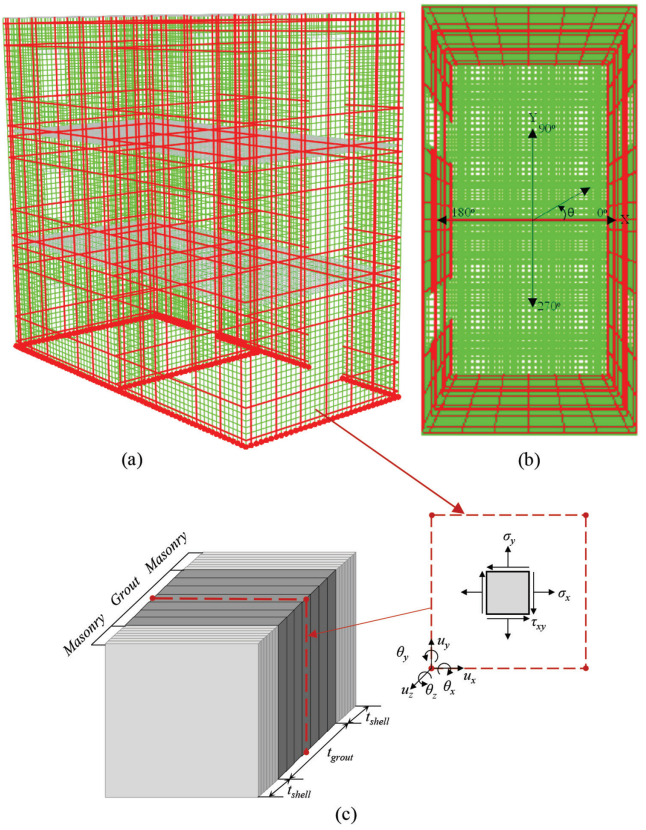

Fig. 2—Finite element mesh: (a) 3-D view; (b) loading direction; and (c) layered shell formulation for one grouted masonry element.

of the model validation are reported in Noor-E-Khuda and Dhanasekar.[51]

Material properties of the block, grout, and steel considered for the prototype building are identical to those used in Abboud et al.[23] Double-cored hollow concrete blocks of dimensions 396 x 193 x 143 mm thick with a face shell thickness of 31 mm were considered in all the walls. A premixed grout consisting of one part of Type II portland cement, three parts of sand, and two parts of 10 mm pea gravel coarse aggregate by volume was considered. The compressive strength and the strain corresponding to the maximum stress in the masonry were 11 MPa and 0.0013, and those of the grout were 18 MPa and 0.0018, respectively. The modulus of rupture of the grout was 1.9 MPa, just over 10% of its compressive strength (18 MPa). Steel reinforcement was considered Grade 60 steel; the yield stress, modulus of elasticity, and yield strain were 462 MPa, 174 GPa, and 0.00267, respectively. The EFE model was shown to accurately predict the deformation, failure, and ultimate capacity of in-plane[14] and out-of-plane[28,48,51] loaded RM walls.

FE building model

The FE mesh of the building model is shown in Fig. 2. The three-dimensional (3-D) model consisted of a total of 15 walls and three floor/roof slabs.

Each component wall of the prototype building was modeled separately using the layered shell element (S4R), shown in Fig. 2(c). The wall-wall and wall-slab-wall interfaces were simulated as perfectly bonded using the

Table 1—Finite element mesh detail of component walls

Component	Element	Node	DOF
Wall AC	1346	1466	8796
Wall DF	1234	1354	8124
Walls CD, BE, and AF	704	759	4554

tie constraint. One of the primary challenges in modeling RM walls is achieving computational economy due to the complications inherited with different materials. To ensure both computational economy and accuracy, the vertical and horizontal reinforcements were discretely modeled using truss elements tied to the nodes of the S4R shell elements. The meshing details of the full building model with the discrete reinforcements are shown in Fig. 2(a). The loading directions on the x-axis (θ = 0, 180 degrees) and y-axis (θ = 90, 270 degrees) are shown in Fig. 2(b). A mesh sensitivity study was performed and a square mesh size of 100 mm was used in the EFE model. There were 20,238 elements, 21,375 nodes, and 128,250 degrees of freedom (DOFs) in the FE building model. Meshing details of the component walls are given in Table 1. Because the connection between the adjacent walls and between the wall and the foundation/slab were modeled using tie constraints, modeling the lap splice, development length, and anchorage of reinforcement was not required in the FE model. Under lateral loading, the concrete slabs were expected to act as a rigid diaphragm; hence, it was modeled using R3D4 rigid elements. To simplify the FE model, reinforcement detailing of the slabs was not considered. The bottom horizontal edge of the building marked with the highlighted elements in Fig. 2(a) was fully constrained with all six translational and rotational DOFs arrested to replicate the full moment connection with the bottom slab.

Loading

All the gravitational and lateral load was applied through the rigid-body reference point located at the geometric center of the slab. In the first step, all the superimposed live and dead loads were gradually applied to the respective story level, which was kept constant throughout the analysis. In the second step, lateral displacement-controlled quasi-static loading along the x-axis (θ = 0, 180 degrees) or y-axis (θ = 90, 270 degrees) was applied through the reference point located on each slab, which was linearly increased until the end of the analysis. Each building model was run in the high-performance computing facility with a generous allocation of central processing units (CPUs) for a set period of 48 hours, and the outcomes were analyzed thereafter.

FE individual wall model

Component walls of the prototype building (AC, DF, CD, BE, and AF) were modeled and analyzed separately to ascertain the influence of the end support condition on the structural performance from a real building perspective. The individually analyzed walls were considered as part of the ground-floor level of the prototype building, as theoretically the ground-floor walls are expected to encounter the

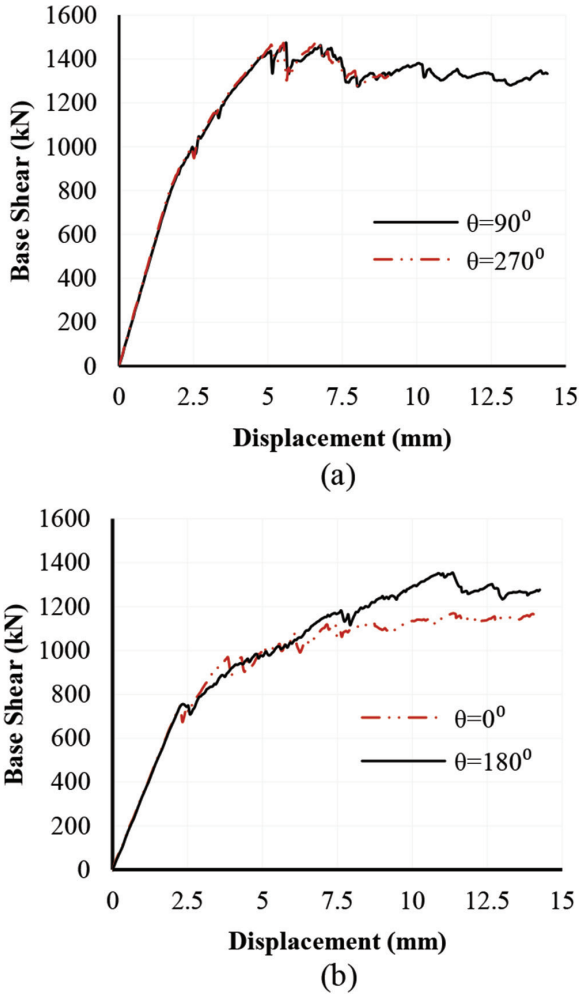

Fig. 3—Load-top floor displacement plot when loaded along: (a) y-axis; and (b) x-axis.

majority of the applied lateral loading. The individual walls were modeled with the same geometric and support arrangements as shown in Fig. 2. An additional precompression loading of 0.33 MPa was applied along the top horizontal edge of the individually analyzed walls to compensate for the gravitational load from the stories above.

STRUCTURAL PERFORMANCE OF PROTOTYPE BUILDING

The structural performance of the prototype building is presented in this section. Key parameters used in the structural response assessment—that is, load capacity, stiffness, ductility, failure modes, deformation profile, reinforcement stress-strain, and mode shapes—are discussed.

Load displacement

Figure 3 shows the lateral load-top floor displacement plot obtained from the FE analysis. The lateral load presented along the vertical axis of the plot is the sum of the reaction forces of the component walls at the ground-floor level of the building. It can be seen that the FE model rationally predicted the lateral load capacity of the prototype building along the different loading directions. The predicted ultimate capacity of the prototype building when loaded along x- and y-axis

Table 2—Displacement ductility and stiffness of building

Direction	V_u, kN	$0.8V_u$, kN	Δ_{max}, mm	Δ_y, mm	k, k N/mm	μ
x-axis	1170	936	14.1	3.6	260	3.92
y-axis	1481	1184.8	14.4	3.4	435.6	4.24

Table 3—Design base shear as per AS 1170.4-2007

Location	Z_{sit}	V_u, kN	Location	Z_{sit}	V_u, kN
Adelaide	0.1	176.1	Perth	0.09	158.5
Brisbane	0.08	140.9	Sydney	0.08	140.9
Darwin	0.09	158.5	Christmas Island	0.15	352.1
Melbourne	0.08	140.9	Cunderdin	0.22	516.4

directions was 1170 and 1481 kN, respectively. The critical loading direction was along the x-axis, where the building offered the least lateral resistance (21% lower than the y-axis direction). It was also observed that the building model was relatively insensitive to the changes in loading direction—that is, θ = 90 and 270 degrees. Such a phenomenon can be explained by the fundamental load distribution mechanism of shear-wall structures. Because no notable changes in the structural stiffness occurred due to alteration of the loading directions (θ = 90 and 270 degrees), the structural performance remained identical. In contrast, a notable difference of 13.6% in the lateral load capacity was observed when the building was loaded along θ = 0- and 180-degree directions.

Structural behavior

The influence of the loading direction on the structural performance of the prototype building is discussed in this section. Key structural performance parameters—namely, the ultimate load capacity, yield and ultimate displacement, stiffness, and ductility demand—of the building were measured for the seismic performance assessment, which is shown in Table 2.

The definitions of the ultimate base shear capacity (V_u), maximum top-floor displacement (Δ_{max}), and the displacement corresponding to 80% of the load capacity (Δ_y, Δ_u) used in the structural performance assessment are shown in Fig. 4.

The design base shear demand of a similar structure constructed at different locations in Australia was measured within the provisions outlined in AS 1170.4, which are given in Table 3. The base shear demand demonstrates the adequacy of the adopted design in the prototype building.

The Australian standard for earthquake design, AS 1170.4, defines the earthquake design category (EDC) within a range of I to III. The base shear (V_u) is estimated using a set of equations, which primarily considers the: 1) structural importance level; 2) site location; 3) subsoil classification; and 4) height of the structure. To calculate V_u, both EDC I and EDC II were used, as both EDCs are applicable to structures of height within 12 to 15 m and situated at a low to moderate earthquake risk zone. The EDC I and EDC II categories adopted the equivalent static force method, where the lateral load is defined either as a fraction of the seismic weight ΣW_i—that is, 10% for EDC I, as shown in Eq. (1), or

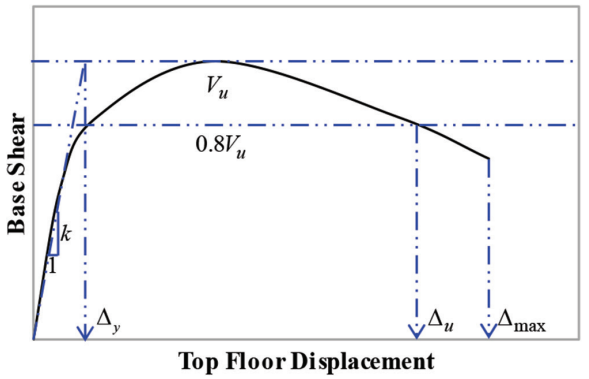

Fig. 4—Idealized load-displacement curve.

the lateral load is calculated using simplified/detailed calculations for EDC II, given in Eq. (2). The demand base shear given in Table 3 is the higher value obtained from the EDC I and EDC II guidelines

$$V_u = \Sigma V_i = \Sigma 0.1 W_i \tag{1}$$

$$V_u = \Sigma V_i = \Sigma W_i k_s k_p Z_{sit} S_{per} / \mu \tag{2}$$

where k_s, k_p, Z_{sit}, and S_{per} are factors accounting for the number of floors and soil type, probability, site hazards, and structural performance of the system, respectively.

The in-plane demand load of the individual walls ($V_{u,i}$) was computed as the sum of the in-plane load acting on the i-th wall (P_i) and the in-plane load on the i-th wall caused by eccentricity ($P_{i,e}$), using Eq. (3) and (4), respectively

$$P_i = V_u \frac{L_i^3}{\Sigma L_i^3} \tag{3}$$

$$P_{i,e} = \frac{V_u e L_i^3 x_i}{\Sigma L_i^3 x_i^2} \tag{4}$$

where the parameters S_i and x_i refer to the horizontal distance of the i-th wall from the edge of the structures and the horizontal distance from the center of rigidity, respectively; L_i refers to the length of the i-th wall; and e represents the loading eccentricity, which is calculated using Eq. (5)

$$e = \frac{(S_i)_{max}}{2} - \frac{\Sigma L_i^3 S_i}{\Sigma L_i^3} \tag{5}$$

The in-plane capacity $V_{d,i}$ of the i-th wall is calculated using Eq. (6), where $A_{d,i}$, $A_{s,i}$, and H_i refer to the design cross-sectional area, area of reinforcement, and height of the i-th wall, respectively.[1]

$$V_{d,i} = \left(1.5 - \frac{H_i}{2L_i}\right) A_{d,i} + 0.8 A_{s,i} f_y \tag{6}$$

Based on the results shown in Fig. 3 and Table 3, it is obvious that the adopted structural design satisfactorily meets the design seismic load demand in all the major

Australian metropolitan/regional areas. The critical lateral load capacity of the ground-floor walls of the prototype building was 126% higher than the design base shear predicted for a similar structure constructed in Cunderdin, WA, Australia.

Stiffness

Stiffness is another key parameter that regulates the structural performance under lateral loading—that is, load-transfer mechanism, mode shape, frequency, and period of vibration. Stiffness is a measure to which the structure resists deformation to applied forces. The stiffness of the building structure primarily depends on the structural arrangement, component wall dimensions, and their end support conditions. A stiffer structure offers higher resistance to lateral loading and displacement. In this study, the stiffness of the prototype building and its component walls were calculated using Eq. (7).

$$k = V_u / \Delta_y \tag{7}$$

From the outcomes presented in Table 2 and Fig. 3, it is evident that the FE model sensibly predicted the structural stiffness of the prototype building. The stiffness of the structure parallel to the longer walls (y-direction) was 67.3% higher than the structure parallel to the shorter walls (x-direction).

Ductility

Displacement ductility refers to the ability of the structure to undergo post-yield deformation without significant loss in strength. This repeated inelastic deformation permits energy dissipation of an earthquake into the structural elements, allowing for a reduction in the design seismic load. The displacement ductility (μ) of the prototype building was measured using the procedure proposed by Park,[52] which is shown in Eq. (8).

$$\mu = \Delta_u / \Delta_y \tag{8}$$

From Table 2, it is obvious that the design detail adopted in this study provided sufficient ductility to the prototype building, which is well above the limiting value of $\mu = 2.0$ (AS 1170.4). The displacement ductility of the prototype building along the x- and y-axis directions was 3.92 and 4.24, respectively. It should be noted that the ductility measurements are conducted based on the structural performance of the walls under static loading. The appropriateness of using the macro-modeling technique with homogenized masonry material properties in assessing the structural performance under cyclic loading is debatable; as such, it is not attempted in this work. Moreover, the quasi-static loading protocol is also used by Dhanasekar and Haider[14] and Abboud et al.[23] in measuring the ductility of RM walls.

Failure modes

A brief overview of the structural damage of the prototype building is shown in Fig. 5. The logarithmic strain that developed in all three stories of the structure at the end of the analysis is presented in the figure. Figures 5(a) to (d) show the structure after it was loaded along θ = 90-, 270-, 0-, and 180-degree directions, respectively.

The prototype building exhibited a similar failure pattern when loaded along both y-axis directions—that is, θ = 90 and 270 degrees—as shown in Fig. 5(a) and (b). As shown in Fig. 5(a), the building primarily cracked next to the openings and at the wall-wall interface near the heel of walls AC and BF (corresponding to a lateral load of 994 kN and a roof displacement of 2.42 mm, as shown in Fig. 3(a)). With the further application of lateral displacement (5.11 mm roof displacement), tensile uplift near the bottom course of wall CD in an out-of-plane mode and at the heel of walls AC and BF in an in-plane mode was detected. Heavy damage to the structure was observed as the roof displacement exceeded 6.9 mm; splitting at the wall-slab-wall interface (near the intersection of walls AC and CD and walls CD and DF) at the ground-floor (roof slab) level and a dense array of diagonal strain lines on the masonry located on both sides of all the door and window openings took place in this stage. At the same time, cracking at the wall-slab-wall interfaces at all levels of the structure (except the top-floor roof) and cracking along the bottom course of walls BE and CD was also observed. It is evident that the ground-floor walls of the structure endured the maximum damage due to in-plane loading; however, crack formations on the other stories of the building could be detected. A similar failure pattern for RM buildings was also observed by Tomaževič and Weiss[53] and Stavridis et al.[54]

The prototype building demonstrated a different failure pattern when loaded along both x-axis directions, as shown in Fig. 5(c) and (d). In this case, the structural damage was primarily limited to the ground-floor region only. Failure of the walls (when loaded along the θ = 0 degrees direction) initiated with the formation of bed-joint cracks next to the window openings on wall AC at a corresponding roof displacement of 2.35 mm. The bed-joint crack propagated to the wall-wall interface between walls AC-CD and AC-AF when the roof displacement was 3.58 mm. Under increased loading, the bed-joint cracks propagated into the adjacent in-plane walls CD, BE, and AF. Other features observed during the analysis include cracking along the bottom course of walls AC, CD, and AE; formation of diagonal cracks on walls CD, BE, and AF; and thicker strain lines all over walls AC, BF, CD, BE, and AF at a corresponding roof displacement of 10.7 mm.

Figure 6 shows the logarithmic strain plot of the individually analyzed FGRM walls. It can be seen that the primary failure mode of the individually analyzed walls, despite the slightly lighter strain concentration, resembled the component walls of the prototype building. A similar failure mode for RM walls with openings was also observed by Stavridis et al.[54] and Voon and Ingham.[55] Notable changes to the failure mode of wall CD were also observed.

Figure 7 shows the kinetic energy versus roof displacement curve alongside the load-displacement response obtained from the respective analysis.

The sudden rise in the kinetic energy, shown in Fig. 7, indicates energy release due to crack formation in the building, which is associated with the sharp drop in load capacity. It

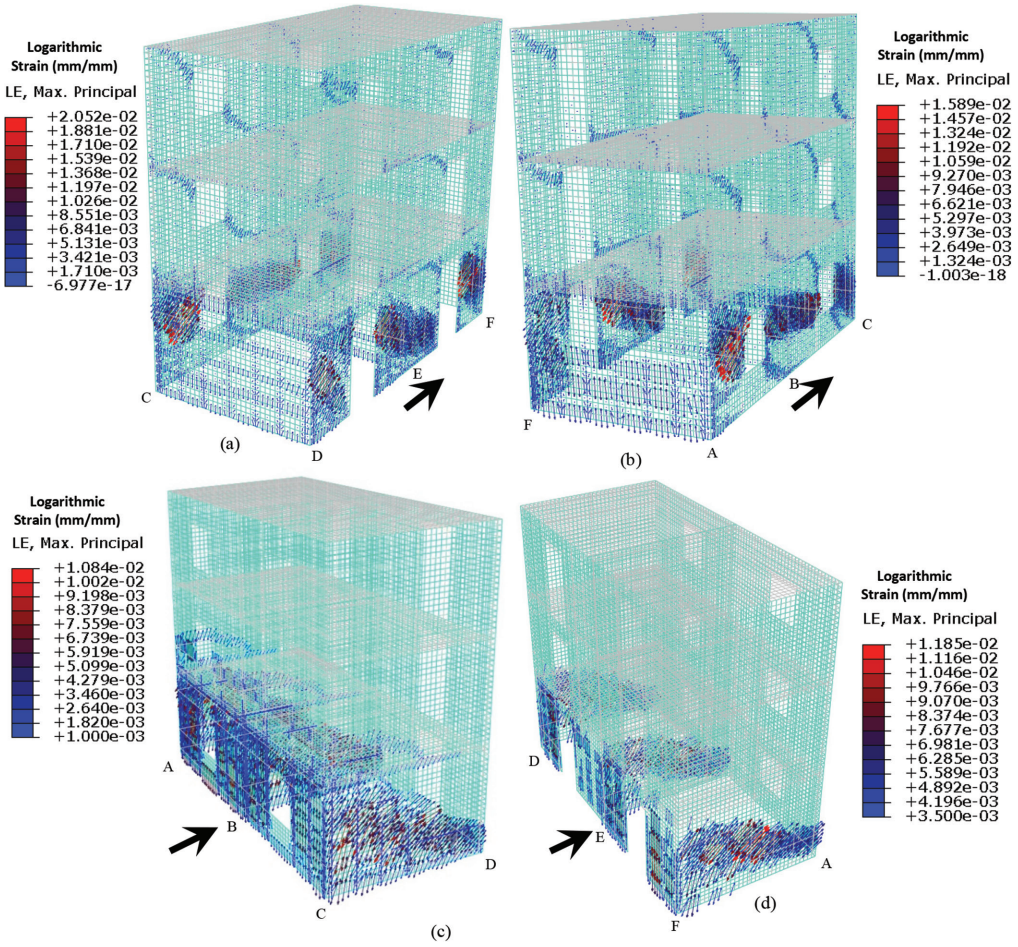

Fig. 5—Logarithmic strain plot of building loaded along: (a) θ = 90 degrees (y-axis); (b) θ = 270 degrees (y-axis); (c) θ = 0 degrees (x-axis); and (d) θ = 180 degrees (x-axis).

can be seen that the kinetic energy plot well picked the structural damage events of the building. The increased number of spikes in the kinetic energy plot correspond to the heavy damage endured by the prototype building when the load was applied along the x- and y-directions.

Figures 8(a) and (b) show the plastic energy dissipation versus the roof-displacement curve of the prototype building when loaded along the y- and x-direction, respectively. Both analyses show that the prototype building demonstrated an elastic behavior up to a corresponding roof displacement of approximately 2.4 mm, while the plastic energy dissipation significantly increased as the roof displacement exceeded 6.9 mm.

Deformation profile

Figure 9 shows a midspan slice taken from the prototype building that represents the vertical deformed shape under the applied lateral loading. In this case, the figure demonstrates the structure loaded along the y-axis direction (θ = 90 degrees).

The deformation profile, shown in Fig. 9(a), closely resembles the idealized displaced shape of the structure[56-59] formed purely through rigid-diaphragm action. The quasi-static displacement applied to the top of the structure resulted in a gradually increasing drift pattern along the height of the structure. It is worth noting that small displacement along the orthogonal direction (x-direction) of the in-plane loaded structure was recorded and that induced torsion to the structural system (as shown in Fig. 9(b)). The difference in stiffness between walls AC and DF caused a small eccentricity between the center of the stiffness of the walls and the geometric centerline of the building that led to the torsional component. The developed rotation is an example of a multidirectional loading scenario (combined in-plane, out-of-plane, and compression[27]), which is commonly experienced in residential masonry buildings.

Reinforcement stress

Figures 10(a) and (b) show the stress experienced by the vertical and horizontal reinforcements of the building when loaded along the θ = 90- and 180-degree directions, respectively. It is clear that the horizontal reinforcements of the in-plane loaded walls (walls AC and DF in Fig. 10(a) and walls CD, BE, and AF in Fig. 10(b)) experienced comparatively higher stress than the vertical reinforcements. On the other hand, the vertical reinforcements in the out-of-plane loaded walls (walls CD, BE, and AF in Fig. 9(a) and walls AC and DF in Fig. 10(b)) experienced higher stress than the horizontal reinforcements.

Figures 11(a) and (b) show the reinforcement stress-strain plot of the in-plane and out-of-plane loaded walls, respectively. The reinforcement stress-strain was measured at the

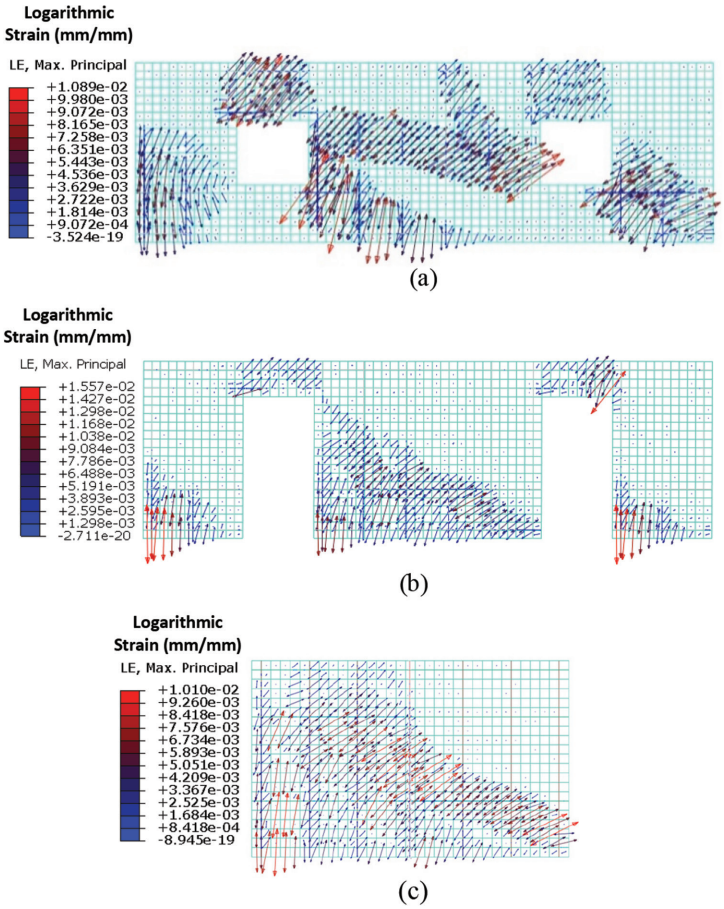

Fig. 6—Logarithmic strain plot of individually analyzed walls: (a) AC; (b) DF; and (c) CD.

location where the reinforcement experienced the maximum strain. For the in-plane and out-of-plane loaded walls with an opening (AC and DF), the stress-strain was measured on the horizontal reinforcement next to the edge of the opening and the vertical reinforcement along the wall bottom, respectively. The same measurements on the solid wall CD were taken on the horizontal reinforcement at the toe of the wall and the vertical reinforcement at the heel of the wall, respectively. From Fig. 11(a), it can be seen that the horizontal reinforcement in all the in-plane loaded walls experienced a considerable amount of stress and tend to reach the steel yield stress (f_y) of 460 MPa and strain of 0.0026.[56] A similar horizontal reinforcement strain was also recorded by Nolph and ElGawady[4] (refer to Fig. 14 and Fig. 17(b) in that paper). The horizontal steel in wall DF reached the post-yield plastic zone, which can be linked to the heavy cracking of the wall next to the door openings. The vertical reinforcement in the out-of-plane loaded walls AC and DF also reached the post-yield plastic zone. The vertical reinforcements in the solid wall CD experienced a comparatively low level of stress (that is, 300 MPa) in the out-of-plane mode. From Fig. 10 and 11, it is apparent that the horizontal and vertical reinforcements of the prototype building contributed to the lateral load-resisting mechanism, which aligns with the contribution of the main reinforcement in the lateral load capacity calculation considered by the AS 3700 design equation, shown in Eq. (6).

Effect of wall thickness

Two additional identical prototype building models with wall thicknesses of 90 and 190 mm (t = 90 and 190 mm) were created and analyzed, where only the thickness of the grouted core was altered, while the thickness of the face shell was kept the same as the original model—that is, 31 mm.

From Fig. 12, it can be seen that the building model with t = 190 mm recorded 28.15% and 28.68% higher load capacity than the building model with t = 143 mm when loaded along the y-axis and x-axis directions, respectively. On the other hand, the building model with t = 90 mm recorded 47.05% and 36.48% lower load capacity than the building model with t = 143 mm when loaded along the y-axis and x-axis directions, respectively.

STRUCTURAL PERFORMANCE OF COMPONENT WALLS

The structural performance of the component walls of the prototype building and equivalent individually analyzed walls is presented in this section. The structural performance of the ground-floor walls is reported only as they encountered the maximum damage.

Longer walls AC and DF

Figure 13 shows the in-plane load-displacement plot of the longer walls AC and DF. The results shown are taken from the structure loaded along the y-axis—that is, θ = 90 and 270 degrees (in-plane to the longer walls)—direction only.

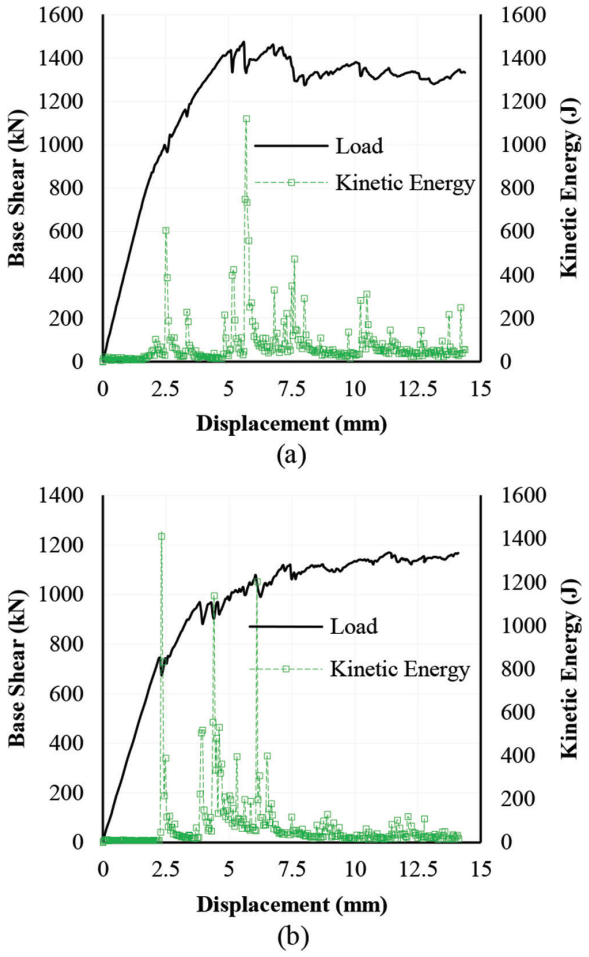

Fig. 7—Kinetic energy and base shear, loaded along: (a) y-axis; and (b) x-axis.

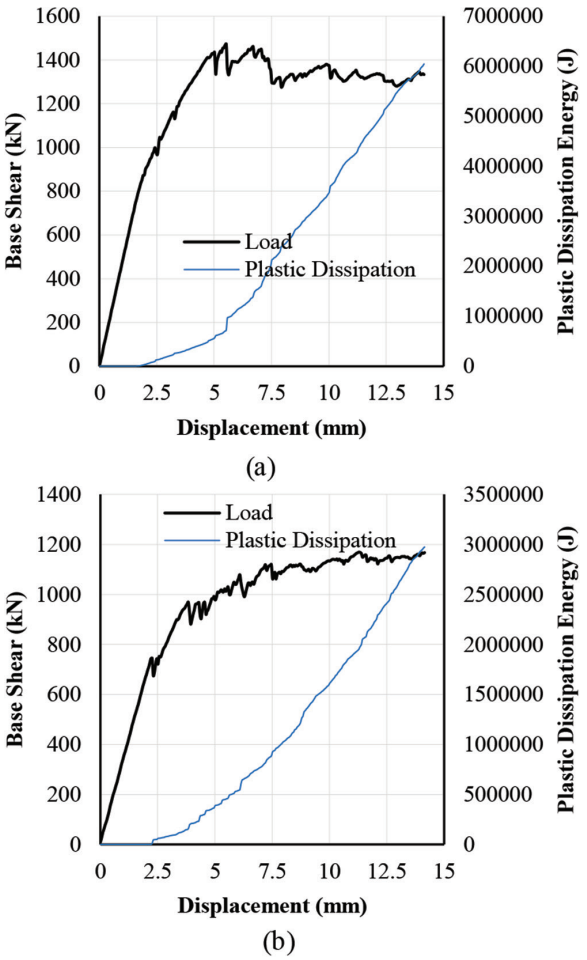

Fig. 8—Plastic energy dissipation and base shear, loaded along: (a) y-axis; and (b) x-axis.

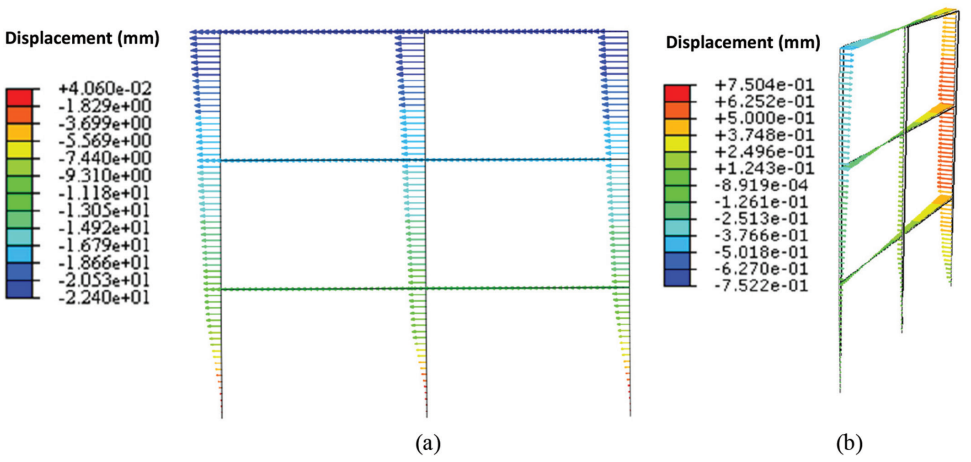

Fig. 9—Deformation profile: (a) displacement of mid-plane slice; and (b) torsion.

The load reported in Fig. 13 is the reaction force of the component walls extracted from the prototype building model. The in-plane displacement was measured at the ground-floor roof level that enabled a justifiable comparison with the individually analyzed walls. It was found that the longer walls AC and DF carried the maximum portion (98%) of the base shear—that is, 758 and 624.75 kN, respectively. Loads resisted by walls CD, BD, and AF in the out-of-plane mode were comparatively low; hence, they were not reported.

The outcomes in Fig. 13 also demonstrate that the structural performance of walls AC and DF was insensitive to the positive/negative in-plane loading direction. Wall AC had an identical end support condition and stiffness at both ends of the wall, which caused unnoticeable changes to the load-displacement plot due to alteration of the loading direction (θ = 90 and 270 degrees). The same was also observed in the case of wall DF. The analysis sensibly predicted that the higher in-plane load was resisted by the stiffer wall; walls

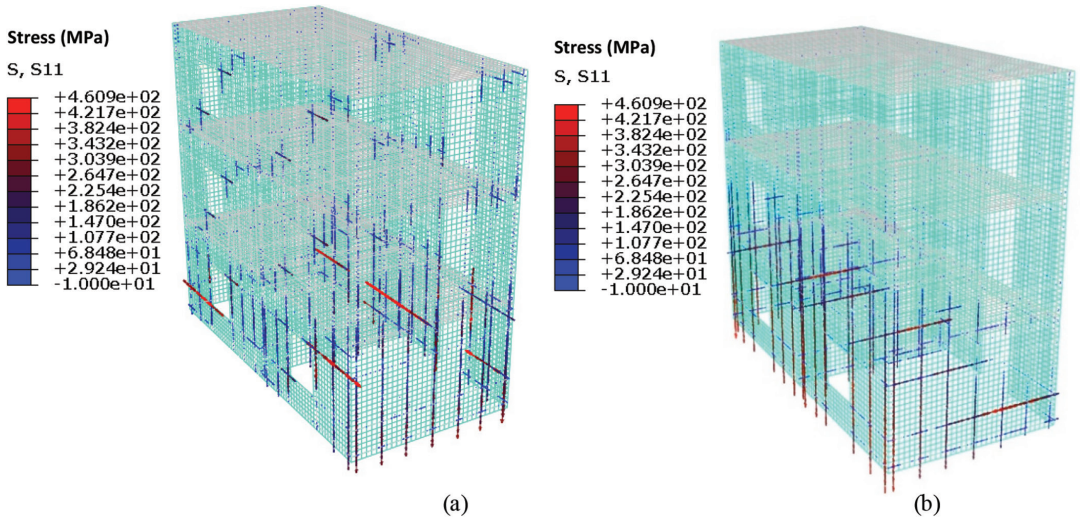

Fig. 10—Reinforcement stress: (a) θ = 90 degrees; and (b) θ = 180 degrees.

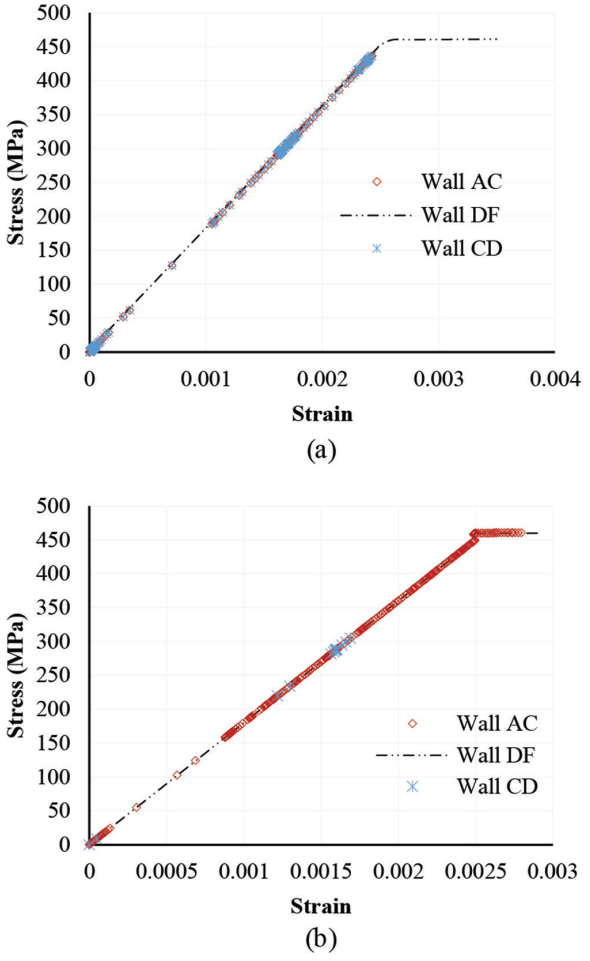

Fig. 11—Reinforcement stress-strain plot: (a) in-plane loaded walls; and (b) out-of-plane loaded walls.

AC and DF attracted 53.7% and 44.3% of the base shear, respectively. Other key structural performance parameters of walls AC and DF derived from the analysis are structural stiffness *k* (478.1 and 428.41 kN/mm, respectively) and displacement ductility μ (3.5 and 2.9, respectively).

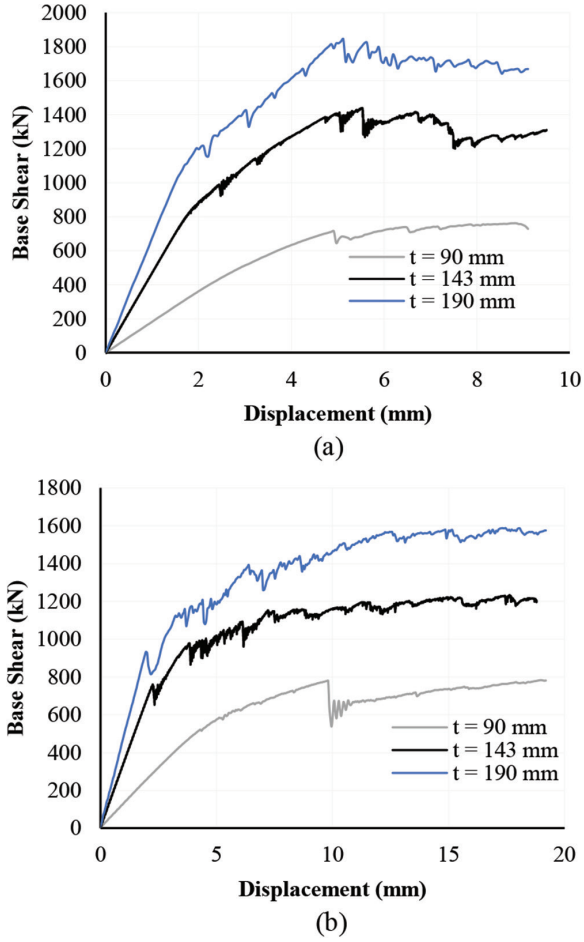

Fig. 12—Load-top floor displacement plot of building model with varying wall thickness, loaded along: (a) y-axis; and (b) x-axis.

Shorter walls CD and BF

Figure 14 shows the load-displacement plot of the shorter walls CD and BF loaded along the θ = 0- and 180-degree directions.

The major portion (approximately 89.7%) of the lateral load on the prototype building was resisted through the

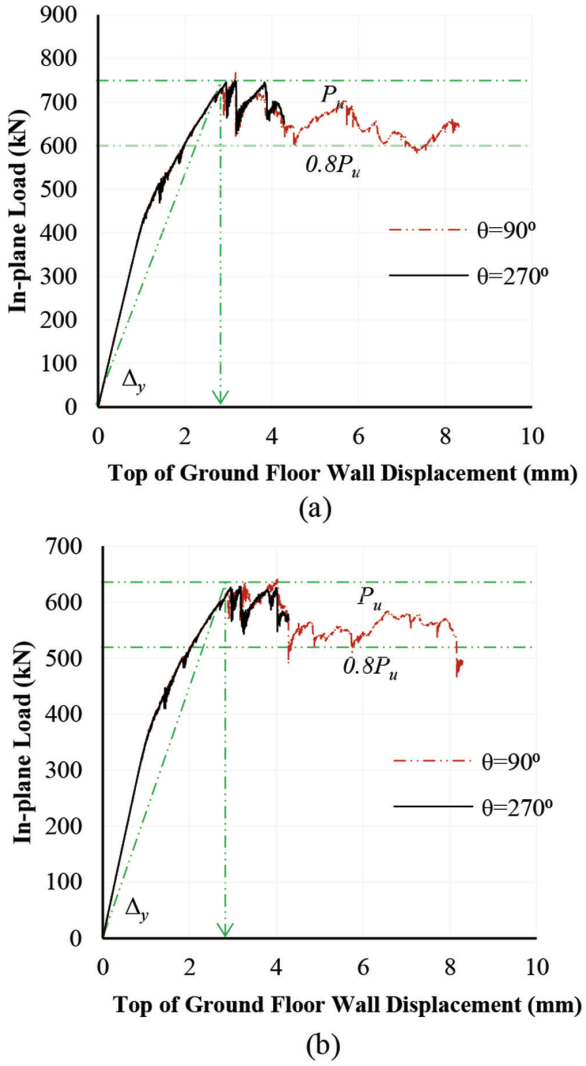

Fig. 13—Load-displacement response of walls loaded along x-axis: (a) wall AC; and (b) wall DF.

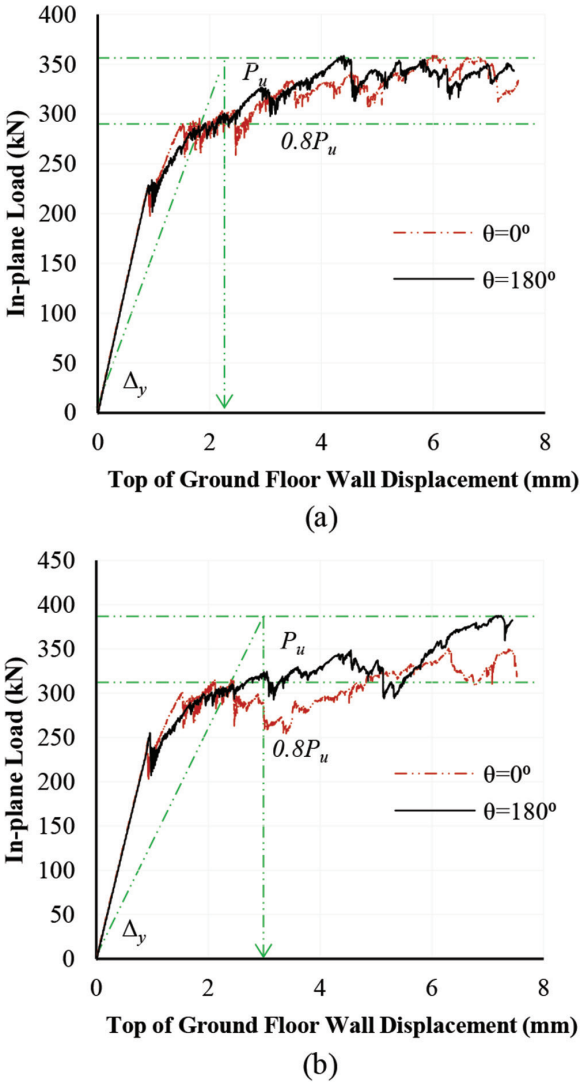

Fig. 14—Load-displacement response of walls loaded along y-axis: (a) wall CD; and (b) wall BE.

in-plane mechanism by walls CD, BE, and AF under this loading case. All the 4 m long walls showed similar behavior up to the peak point and attained a similar ultimate load capacity of approximately 350 kN irrespective of the positive/negative loading direction. Interior wall BE was found to be stiffer over the exterior wall CD; the lateral stiffness of walls BE and CD were 307.6 and 301.7 kN/mm, respectively. The higher (initial) stiffness of wall BE was due to the stronger end support provided by the orthogonal walls that acted as flanges spanning both sides of the main web wall (similar to H-shaped walls) over wall CD, where the flange extruded to one side of the web only (forming a C-shaped geometry). A notable variation in the post-peak softening response was observed due to alteration of the loading direction. The different stiffness provided at the opposite wall ends by the support walls AC and DF perhaps affected the post-yield behavior of the shorter walls. It was also observed in Fig. 5 that only one of the two longer out-of-plane loaded walls failed when loaded alternatively along the θ = 0- and 180-degree directions, which contributed to the variation in the post-peak response. Displacement ductility of the exterior wall CD was higher (μ = 3.17) than that of interior wall BE (μ = 2.43).

Individual wall analysis

Figure 15 shows a comparison of the load-displacement relation of the component walls to equivalent individually analyzed walls. Key structural features of these walls including load capacity, stiffness, and ductility are reported in Table 4.

A comparison of the load-displacement performance of walls AC and DF to equivalent individually analyzed walls is shown in Fig. 15(a) and (b), respectively. As already discussed, these walls are taken from the ground-floor level of the building. To provide a further explanation of their structural performance, each plot is broadly divided into three zones—that is, zones (I), (II), and (III). Zone (I) falls within the linear elastic domain of the curve, where the load-displacement response of the component and the individually analyzed walls are parallel to each other. Zones (II) and (III), on the other hand, depict the vital changes in the performance, highlighting the strength gain path to the peak and the post-peak inelastic behavior, respectively.

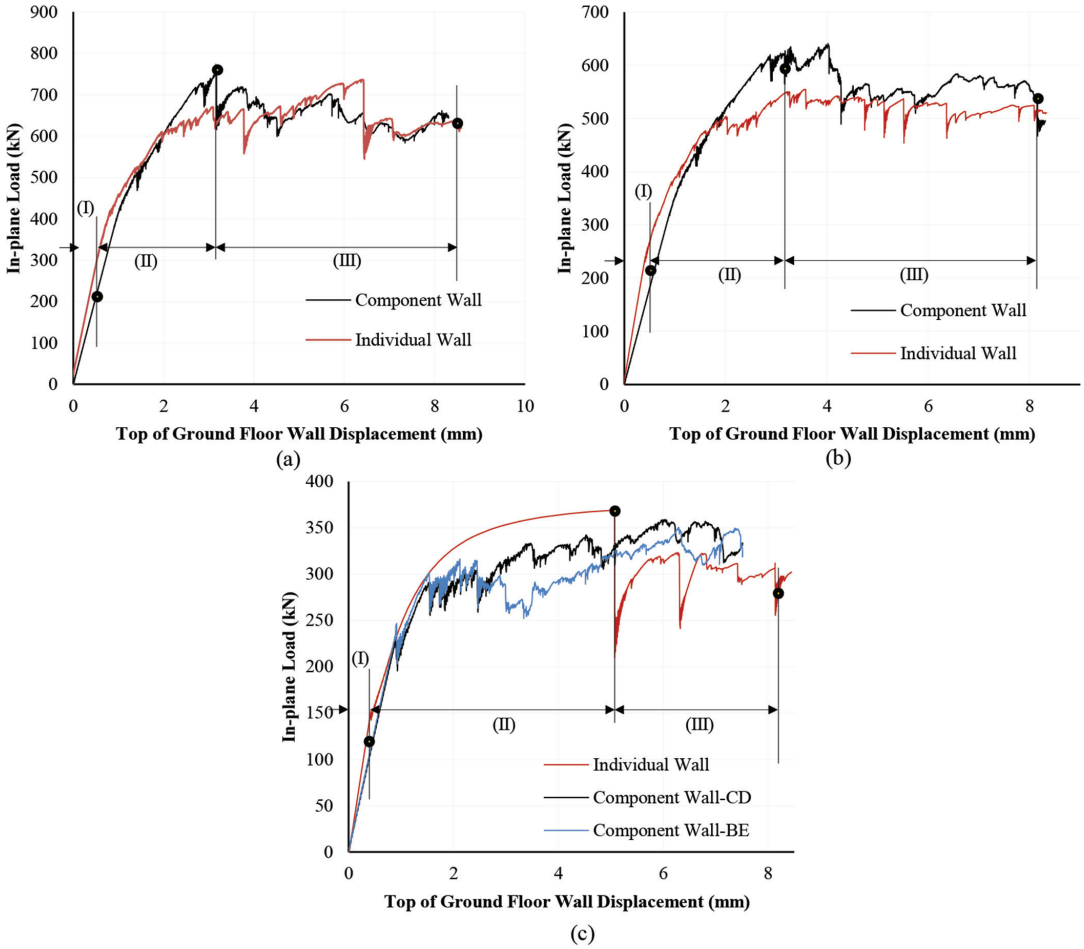

Fig. 15—Comparison of load-displacement response of individual walls with component walls: (a) wall AC; (b) wall DF; and (c) walls CD and BE.

Table 4—Structural performance of component and individual walls

Wall	Type	$V_{u,i}$, kN			k, kN/mm	Δ_{max}	μ
		EFE	AS 1170.4	AS 3700			
AC	Component	758	274.3	1721.3	478.1	8.32	3.5
	Individual	736.1			462.19	8.49	3.95
DF	Component	624.75	232.2	1113.8	428.41	8.2	2.9
	Individual	548			391.01	8.25	4.58
CD	Component	354	141.04	821.3	307.6	7.41	3.17
	Individual	362			333.3	8.5	4.29
BE	Component	387	141.04	821.3	301.7	7.63	2.43
	Individual	362			333.3	8.5	4.29

Zone (II) represents a combination of the linear and nonlinear portion of the curve associated with a substantial increase in the load capacity. Only the component walls of the prototype building reached the peak capacity within this zone. The visible gap between the slopes of the individually analyzed and component walls illustrates the difference in the structural stiffness of the walls under consideration. Based on the results shown in Fig. 15, and Table 4, it is evident that the walls designed and analyzed separately as individual walls will be less stiff than the similar component walls of the prototype building. On a similar note, the individual walls, when in a real building, will result in additional unidentified stiffness and consequently can attract unexpectedly higher seismic loads. The additional stiffness to the RM wall structural system is from the partial/full end moment resistance provided by the orthogonally positioned support walls. It is also evident that AS 1170.4 counterbalances such unidentified stiffness by setting the same structural performance factor $S_{per} = 0.77$ for both unreinforced masonry and RM walls.

Zone (III) primarily constitutes the structural response to cracking of the main and adjacent support walls on the load-displacement relation. The zone extends all over the

post-peak softening range of the load-displacement curve. It can be seen that the component walls from the prototype building suffered a marginal loss in load capacity after the stiffer jump in Zone (II).

Figure 15(c) shows a comparison of the load-displacement performance of the component and individually analyzed solid walls CD and BE. Component walls CD and BE failed at a lower level of in-plane load than similar walls when analyzed individually. From Fig. 15(c), it can be seen that both the individually analyzed and component walls followed the same path within the elastic domain (Zone (I)) of the load-displacement curve. However, the component walls experienced several drops in the load capacity within Zone (II), which is linked to the crack widening in the adjacent walls/supported ends. As already discussed in the "Failure modes" section, the cracks from the adjacent support walls propagated to the main walls, especially those situated next to the window openings (walls CD and BE); hence, numerous sharp spikes (due to the crack formations) on the load-displacement curves were identified for the component walls. In contrast, the structural performance of individually analyzed solid wall CD was not affected by such a cracking phenomenon. The individually analyzed wall smoothly reached the peak load and then experienced extensive cracking and a drop in the in-plane capacity in Zone (III).

Based on the results shown in Fig. 5(c) and (d), 11, and 15 and Table 4, it is apparent that the shorter walls CD and BE suffered the maximum loss in post-yield capacity due to the cracking of the adjacent support walls (AC and DF) with openings. Structural performance obtained through the individually analyzed walls (especially for walls CD and BE) raises the concern of a superficial rise in the load capacity, which did not occur in the case of the prototype building. Figure 16 shows a comparison of the in-plane capacity ($V_{u,i}$) of the solid RM wall CD to the capacity of RM walls reported by Nolph and ElGawady,[4] Shing et al.,[5] Voon and Ingham,[6] and Shedid et al.[7] Because the walls were distinct in terms of their dimensions, material properties, reinforcing details, and load application method, the $V_{u,i}$ of each wall was divided by its length (L_i) and height (H_i) dimension to measure the in-plane capacity offered by a unit surface area of the wall. The horizontal reinforcement ratio of each wall is also presented in Fig. 16. It is observed that the $V_{u,i}/H_iL_i$ value of wall CD is very close (±10%) to that of the RM walls tested by Nolph and ElGawady[4] and Shedid et al.[7] The $V_{u,i}/H_iL_i$ value of walls tested by Shing et al.[5] and Voon and Ingham[6] were comparatively higher than wall CD, which is due to the higher vertical reinforcement ratio, different reinforcement detailing, shear-dominated failure modes, and different aspect ratio ($H_i/L_i \approx 1.0$) of the wall. In general, walls containing a higher reinforcement ratio resulted in a higher $V_{u,i}/H_iL_i$ value.

Table 4 presents the capacities of the component and individually analyzed walls obtained from the EFE model, the maximum design demand load as per AS 1170.4 (for Cunderdin) and the maximum in-plane load capacity predicted by AS 3700 design equations. It is apparent that the adopted design detail of the component walls fulfilled the design demand load capacity requirements, although the AS 3700 code predictions are unacceptable. Such unconservative prediction by the AS 3700 equation was also reported by Janaraj and Dhanasekar.[10,18]

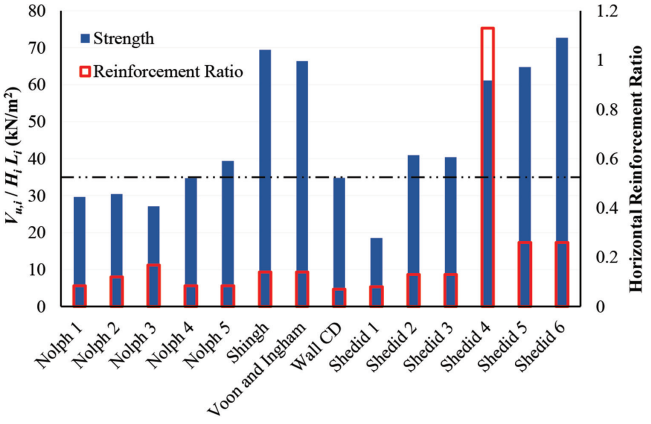

Fig. 16—In-plane capacity of wall CD and walls reported in literature.

CONCLUSIONS

The structural performance of a fully grouted reinforced masonry (FGRM) prototype building designed within the AS 3700:2018 design guidelines is evaluated. The study is conducted using an explicit finite element (EFE) model, where masonry is defined using an elastic-plastic macroscopic material model. The EFE model is used to investigate the influence of loading direction and end support condition on the structural performance of the building in terms of load capacity, stiffness, and ductility. A separate analysis is carried out on equivalent individual walls loaded along the in-plane directions, and the outcomes are compared with the component walls obtained from the prototype building. The following conclusions could be drawn from the study.

- The adopted design detail with a low vertical and horizontal reinforcement ratio provided sufficient load capacity to the prototype building and the component walls against the design demand load. The critical base shear was observed when the building was loaded along the parallel to the shorter wall (without opening) direction (θ = 0 and 180 degrees). The building as a whole and the component walls showed sufficient ductility irrespective of the loading direction.
- The variation of lateral stiffness between the longer walls with window and door openings generated slight eccentricity to the structural system. The positive and negative loading direction mostly affected the inelastic softening response of the load-displacement curve.
- The individually analyzed walls with window and door openings exhibited lower stiffness and ductility over walls acting as components of the prototype building.
- The horizontal and vertical reinforcements experienced yielding in the in-plane and out-of-plane loaded walls, respectively.
- The peak in-plane capacity of the shorter walls without an opening was affected by the crack propagation to the main walls from the adjacent support walls. These walls

suffered severe cracking, as evidenced by the sharp spikes in the load-displacement curve. The individually analyzed walls, on the other hand, showed comparatively less cracking and, as a result, instigated a superficial rise in the capacity, which did not occur in the case of the prototype building. The in-plane capacity of the shorter wall without openings compared well with the in-plane capacity of walls reported in the literature.

- The AS 3700:2018 in-plane design equation for RM walls is highly unconservative and requires immediate review.

AUTHOR BIOS

Sarkar Noor-E-Khuda *is a Senior Lecturer in the School of Engineering and Technology at Central Queensland University, Melbourne, VIC, Australia. He received his PhD from Queensland University of Technology, Brisbane, QLD, Australia, in 2016. His research interests include masonry structures, finite element modeling, and destructive and nondestructive testing.*

ACKNOWLEDGMENTS

The author gratefully acknowledges the computational resources provided by the Central Queensland University research division and the high-performance computing CQUniversity-HPC team.

Some or all data, models, or code that support the findings of this study are available from the corresponding author upon reasonable request.

REFERENCES

1. AS 3700:2018, "Australian Standard of Masonry Structures," Standards Australia, Sydney, Australia, 2018.

2. AS 3600:2018, "Australian Standard of Concrete Structures," Standards Australia, Sydney, Australia, 2018.

3. TMS 402/602-16, "Building Code Requirements and Specification for Masonry Structures," The Masonry Society, Longmont, CO, 2016.

4. Nolph, S. M., and ElGawady, M. A., "Static Cyclic Response of Partially Grouted Masonry Shear Walls," *Journal of Structural Engineering*, ASCE, V. 138, No. 7, 2012, pp. 864-879. doi: 10.1061/(ASCE)ST.1943-541X.0000529

5. Shing, P. B.; Schuller, M.; and Hoskere, V. S., "In-Plane Resistance of Reinforced Masonry Shear Walls," *Journal of Structural Engineering*, ASCE, V. 116, No. 3, 1990, pp. 619-640. doi: 10.1061/(ASCE)0733-9445(1990)116:3(619)

6. Voon, K. C., and Ingham, J. M., "Experimental In-Plane Shear Strength Investigation of Reinforced Concrete Masonry Walls," *Journal of Structural Engineering*, ASCE, V. 132, No. 3, 2006, pp. 400-408. doi: 10.1061/(ASCE)0733-9445(2006)132:3(400)

7. Shedid, M. T.; El-Dakhakhni, W. W.; and Drysdale, R. G., "Behavior of Fully Grouted Reinforced Concrete Masonry Shear Walls Failing in Flexure: Analysis," *Engineering Structures*, V. 31, No. 9, 2009, pp. 2032-2044. doi: 10.1016/j.engstruct.2009.03.006

8. Seif ElDin, H. M., and Galal, K., "Effect of Reinforcement Anchorage End Detail and Spacing on Seismic Performance of Masonry Shear Walls," *Engineering Structures*, V. 157, 2018, pp. 268-279. doi: 10.1016/j.engstruct.2017.11.073

9. Haider, W., and Dhanasekar, M., "Experimental Study of Monotonically Loaded Wide Spaced Reinforced Masonry Shear Walls," *Australian Journal of Structural Engineering*, V. 5, No. 2, 2004, pp. 101-118. doi: 10.1080/13287982.2004.11464931

10. Janaraj, T., and Dhanasekar, M., "Studies on the Existing In-Plane Shear Equations of Partially Grouted Reinforced Masonry," *Australian Journal of Structural Engineering*, V. 17, No. 3, 2016, pp. 180-187. doi: 10.1080/13287982.2016.1240743

11. Bolhassani, M.; Hamid, A. A.; Johnson, C.; Moon, F. L.; and Schultz, A. E., "New Design Detail to Enhance the Seismic Performance of Ordinary Reinforced Partially Grouted Masonry Structures," *Journal of Structural Engineering*, ASCE, V. 142, No. 12, 2016, p. 04016142. doi: 10.1061/(ASCE)ST.1943-541X.0001620

12. El-Dakhakhni, W. W.; Banting, B. R.; and Miller, S. C., "Seismic Performance Parameter Quantification of Shear-Critical Reinforced Concrete Masonry Squat Walls," *Journal of Structural Engineering*, ASCE, V. 139, No. 6, 2013, pp. 957-973. doi: 10.1061/(ASCE)ST.1943-541X.0000713

13. Seif ElDin, H. M., and Galal, K., "In-Plane Seismic Performance of Fully Grouted Reinforced Masonry Shear Walls," *Journal of Structural Engineering*, ASCE, V. 143, No. 7, 2017, p. 04017054. doi: 10.1061/(ASCE)ST.1943-541X.0001758

14. Dhanasekar, M., and Haider, W., "Explicit Finite Element Analysis of Lightly Reinforced Masonry Shear Walls," *Computers & Structures*, V. 86, No. 1-2, 2008, pp. 15-26. doi: 10.1016/j.compstruc.2007.06.006

15. Kasparik, T.; Tait, M. J.; and El-Dakhakhni, W. W., "Seismic Performance Assessment of Partially Grouted, Nominally Reinforced Concrete-Masonry Structural Walls Using Shake Table Testing," *Journal of Performance of Constructed Facilities*, ASCE, V. 28, No. 2, 2014, pp. 216-227. doi: 10.1061/(ASCE)CF.1943-5509.0000416

16. Minaie, E.; Mota, M.; Moon, F. L.; and Hamid, A. A., "In-Plane Behavior of Partially Grouted Reinforced Concrete Masonry Shear Walls," *Journal of Structural Engineering*, ASCE, V. 136, No. 9, 2010, pp. 1089-1097. doi: 10.1061/(ASCE)ST.1943-541X.0000206

17. Shedid, M. T.; Drysdale, R. G.; and El-Dakhakhni, W. W., "Behavior of Fully Grouted Reinforced Concrete Masonry Shear Walls Failing in Flexure: Experimental Results," *Journal of Structural Engineering*, ASCE, V. 134, No. 11, 2008, pp. 1754-1767. doi: 10.1061/(ASCE)0733-9445(2008)134:11(1754)

18. Janaraj, T., and Dhanasekar, M., "Design Expressions for the In-Plane Shear Capacity of Confined Masonry Shear Walls Containing Squat Panels," *Journal of Structural Engineering*, ASCE, V. 142, No. 2, 2016, p. 04015127. doi: 10.1061/(ASCE)ST.1943-541X.0001403

19. Andolfato, R. P.; Ramalho, M. A.; Corrêa, M. R. S.; and Haach, V. G., "Study of Vertical Load Distribution in Full-Scale Four-Story Masonry Building," *ACI Structural Journal*, V. 111, No. 3, May-June 2014, pp. 685-692. doi: 10.14359/51686626

20. Drysdale, R. G.; El-Dakhakhni, W. W.; and Kolodziejski, E. A., "Shear Capacity for Flange-Web Intersection of Concrete Block Shear Walls," *Journal of Structural Engineering*, ASCE, V. 134, No. 6, 2008, pp. 947-960. doi: 10.1061/(ASCE)0733-9445(2008)134:6(947)

21. Baxter, R. P., "The Out-of-Plane Behaviour of Reinforced Concrete Masonry Walls with Window Openings," Master's thesis, University of Canterbury, Christchurch, New Zealand, 2001.

22. Tomaževič, M., and Klemenc, I., "Seismic Behaviour of Confined Masonry Walls," *Earthquake Engineering & Structural Dynamics*, V. 26, No. 10, 1997, pp. 1059-1071. doi: 10.1002/(SICI)1096-9845(199710)26:10<1059::AID-EQE694>3.0.CO;2-M

23. Abboud, B. E.; Hamid, A. A.; and Harris, H. G., "Flexural Behavior of Reinforced Concrete Masonry Walls under Out-of-Plane Monotonic Loads," *ACI Structural Journal*, V. 93, No. 3, May-June 1996, pp. 327-335.

24. Browning, R. S.; Dinan, R. J.; and Davidson, J. S., "Blast Resistance of Fully Grouted Reinforced Concrete Masonry Veneer Walls," *Journal of Performance of Constructed Facilities*, ASCE, V. 28, No. 2, 2014, pp. 228-241. doi: 10.1061/(ASCE)CF.1943-5509.0000434

25. da Porto, F.; Mosele, F.; and Modena, C., "Experimental Testing of Tall Reinforced Masonry Walls under Out-of-Plane Actions," *Construction and Building Materials*, V. 24, No. 12, 2010, pp. 2559-2571. doi: 10.1016/j.conbuildmat.2010.05.020

26. Noor-E-Khuda, S., and Dhanasekar, M., "Three Sides Supported Unreinforced Masonry Walls under Multi-Directional Loading," *Construction and Building Materials*, V. 188, 2018, pp. 1207-1220. doi: 10.1016/j.conbuildmat.2018.08.144

27. Noor-E-Khuda, S., and Dhanasekar, M., "Masonry Walls under Combined In-Plane and Out-of-Plane Loadings," *Journal of Structural Engineering*, ASCE, V. 144, No. 2, 2018, p. 04017186. doi: 10.1061/(ASCE)ST.1943-541X.0001930

28. Noor-E-Khuda, S.; Dhanasekar, M.; and Thambiratnam, D. P., "Out-of-Plane Deformation and Failure of Masonry Walls with Various Forms of Reinforcement," *Composite Structures*, V. 140, 2016, pp. 262-277. doi: 10.1016/j.compstruct.2015.12.028

29. Lourenço, P. B., "Anisotropic Softening Model for Masonry Plates and Shells," *Journal of Structural Engineering*, ASCE, V. 126, No. 9, 2000, pp. 1008-1016. doi: 10.1061/(ASCE)0733-9445(2000)126:9(1008)

30. Milani, G.; Lourenço, P.; and Tralli, A., "Homogenization Approach for the Limit Analysis of Out-of-Plane Loaded Masonry Walls," *Journal of Structural Engineering*, ASCE, V. 132, No. 10, 2006, pp. 1650-1663. doi: 10.1061/(ASCE)0733-9445(2006)132:10(1650)

31. Koutromanos, I., and Shing, P. B., "Cohesive Crack Model to Simulate Cyclic Response of Concrete and Masonry Structures," *ACI Structural Journal*, V. 109, No. 3, May-June 2012, pp. 349-358.

32. Zhuge, Y.; Thambiratnam, D.; and Corderoy, J., "Nonlinear Dynamic Analysis of Unreinforced Masonry," *Journal of Structural Engineering*, ASCE, V. 124, No. 3, 1998, pp. 270-277. doi: 10.1061/(ASCE)0733-9445(1998)124:3(270)

33. Minaie, E.; Moon, F. L.; and Hamid, A. A., "Nonlinear Finite Element Modeling of Reinforced Masonry Shear Walls for Bidirectional

Loading Response," *Finite Elements in Analysis and Design*, V. 84, 2014, pp. 44-53. doi: 10.1016/j.finel.2014.02.001

34. Voon, K. C., and Ingham, J. M., "Design Expression for the In-Plane Shear Strength of Reinforced Concrete Masonry," *Journal of Structural Engineering*, ASCE, V. 133, No. 5, 2007, pp. 706-713. doi: 10.1061/(ASCE)0733-9445(2007)133:5(706)

35. Seible, F.; Priestley, M. J. N.; Kingsley, G. R.; and Kürkchübasche, A. G., "Seismic Response of Full-Scale Five-Story Reinforced-Masonry Building," *Journal of Structural Engineering*, ASCE, V. 120, No. 3, 1994, pp. 925-946. doi: 10.1061/(ASCE)0733-9445(1994)120:3(925)

36. Ali Shah, S. M.; Shahzada, K.; Gencturk, B.; and Memon, S. A., "Retrofitting of Full-Scale Confined Masonry Building Using Ferro-Cement Overlay," *Journal of Performance of Constructed Facilities*, ASCE, V. 31, No. 5, 2017, p. 04017079. doi: 10.1061/(ASCE)CF.1943-5509.0001060

37. Ezzeldin, M.; El-Dakhakhni, W.; and Wiebe, L., "Reinforced Masonry Building Seismic Response Models for ASCE/SEI-41," *Journal of Structural Engineering*, ASCE, V. 144, No. 1, 2018, p. 04017175. doi: 10.1061/(ASCE)ST.1943-541X.0001914

38. Heerema, P.; Shedid, M.; and El-Dakhakhni, W., "Seismic Response Analysis of a Reinforced Concrete Block Shear Wall Asymmetric Building," *Journal of Structural Engineering*, ASCE, V. 141, No. 7, 2015, p. 04014178. doi: 10.1061/(ASCE)ST.1943-541X.0001140

39. Siyam, M. A.; Konstantinidis, D.; and El-Dakhakhni, W., "Collapse Fragility Evaluation of Ductile Reinforced Concrete Block Wall Systems for Seismic Risk Assessment," *Journal of Performance of Constructed Facilities*, ASCE, V. 30, No. 6, 2016, p. 04016047. doi: 10.1061/(ASCE)CF.1943-5509.0000895

40. El-Dakhakhni, W., and Ashour, A., "Seismic Response of Reinforced-Concrete Masonry Shear-Wall Components and Systems: State of the Art," *Journal of Structural Engineering*, ASCE, V. 143, No. 9, 2017, p. 03117001. doi: 10.1061/(ASCE)ST.1943-541X.0001840

41. Ezzeldin, M.; Wiebe, L.; and El-Dakhakhni, W., "System-Level Seismic Risk Assessment Methodology: Application to Reinforced Masonry Buildings with Boundary Elements," *Journal of Structural Engineering*, ASCE, V. 143, No. 9, 2017, p. 04017084. doi: 10.1061/(ASCE)ST.1943-541X.0001815

42. Ashour, A.; Ezzeldin, M.; and El-Dakhakhni, W., "System-Level Seismic Damage Assessment Methodology for Reinforced Masonry Shear Wall Buildings," *Journal of Structural Engineering*, ASCE, V. 144, No. 8, 2018, p. 04018117. doi: 10.1061/(ASCE)ST.1943-541X.0002091

43. Medeiros, K. A. S.; Chavez, K. H.; Fonseca, F. S.; Parsekian, G. A.; and Shrive, N. G., "Parametric Study of Multi-Story, Perforated, Partially Grouted Masonry Walls Subjected to In-Plane Cyclic Actions," *Canadian Journal of Civil Engineering*, V. 48, No. 8, 2021, pp. 1046-1055. doi: 10.1139/cjce-2020-0128

44. Chavez, K. H., 2018, "Parametric Study on Multi-Story, Partially Grouted, Perforated, Masonry Shear Walls by Finite Element Analysis," Master's thesis, Brigham Young University, Provo, UT, https://scholarsarchive.byu.edu/etd/7059. (last accessed Sept. 13, 2022)

45. Buxton, J. R., 2017, "Strut-and-Tie Modeling of Multistory, Partially-Grouted, Concrete Masonry Shear Walls with Openings," Master's thesis, Brigham Young University, Provo, UT, https://scholarsarchive.byu.edu/etd/6292. (last accessed Sept. 13, 2022)

46. AS 1170.4-2007, "Structural Design Actions – Part 4: Earthquake Actions in Australia," Standards Australia, Sydney, Australia, 2007.

47. Ullah, S. N.; Noor, E.; Noor-E-Khuda, S.; Fook Hou, L.; Suntharavadivel, T.; and Albermani, F., "Deep Undrained Bearing Capacity of Rectangular Foundations in Uniform Strength Clay," *Journal of Geotechnical and Geoenvironmental Engineering*, ASCE, V. 146, No. 10, 2020, p. 04020105. doi: 10.1061/(ASCE)GT.1943-5606.0002356

48. Noor-E-Khuda, S.; Dhanasekar, M.; and Thambiratnam, D. P., "An Explicit Finite Element Modelling Method for Masonry Walls under Out-of-Plane Loading," *Engineering Structures*, V. 113, 2016, pp. 103-120. doi: 10.1016/j.engstruct.2016.01.026

49. Hibbitt, H.; Karlsson, B.; and Sorensen, P., "Abaqus Analysis User's Manual Version 6.10," Dassault Systèmes Simulia Corp., Providence, RI, 2011.

50. Zahra, T.; Thamboo, J.; Asad, M.; and Song, M., "Experimental Investigation on the Effectiveness of Lateral Restrainers to the Vertical Steel in Reinforced Masonry Walls under Axial Compression," *Construction and Building Materials*, V. 297, 2021, Article No. 123790. doi: 10.1016/j.conbuildmat.2021.123790

51. Noor-E-Khuda, S., and Dhanasekar, M., "On the Out-of-Plane Flexural Design of Reinforced Masonry Walls," *Journal of Building Engineering*, V. 27, 2020, Article No. 100945. doi: 10.1016/j.jobe.2019.100945

52. Park, R., "Evaluation of Ductility of Structures and Structural Assemblages from Laboratory Testing," *Bulletin of the New Zealand Society for Earthquake Engineering*, V. 22, No. 3, 1989, pp. 155-166. doi: 10.5459/bnzsee.22.3.155-166

53. Tomaževič, M., and Weiss, P., "Seismic Behavior of Plain- and Reinforced-Masonry Buildings," *Journal of Structural Engineering*, ASCE, V. 120, No. 2, 1994, pp. 323-338. doi: 10.1061/(ASCE)0733-9445(1994)120:2(323)

54. Stavridis, A.; Ahmadi, F.; Mavros, M.; Shing, P. B.; Klingner, R. E.; and McLean, D., "Shake-Table Tests of a Full-Scale Three-Story Reinforced Masonry Shear Wall Structure," *Journal of Structural Engineering*, ASCE, V. 142, No. 10, 2016, p. 04016074. doi: 10.1061/(ASCE)ST.1943-541X.0001527

55. Voon, K. C., and Ingham, J. M., "Experimental In-Plane Strength Investigation of Reinforced Concrete Masonry Walls with Openings," *Journal of Structural Engineering*, ASCE, V. 134, No. 5, 2008, pp. 758-768. doi: 10.1061/(ASCE)0733-9445(2008)134:5(758)

56. Noor-E-Khuda, S., and Thambiratnam, D. P., "In-Plane and Out-of-Plane Structural Performance of Fully Grouted Reinforced Masonry Walls with Varying Reinforcement Ratio–A Numerical Study," *Engineering Structures*, V. 248, 2021, Article No. 113288. doi: 10.1016/j.engstruct.2021.113288

57. Fortes, E. S.; Silva, M. R.; Parsekian, G. A.; Fonseca, F. S.; and Shrive, N. G., "Quasi-Static Cyclic Testing of Partially Grouted Masonry Walls with Openings—Preliminary Results," *Brick and Block Masonry: Proceedings of the 16th International Brick and Block Masonry Conference*, Padua, Italy, June 26-30, 2016, pp. 187-194.

58. Fortes, E. S.; Parsekian, G. A.; Fonseca, F. S.; and Shrive, N. G., "Influence of Openings on Quasi-Static Cyclic Behaviour of Partially Grouted Masonry Walls," *13th Canadian Masonry Symposium*, Halifax, NS, Canada, 2017, 11 pp.

59. Cheng, J.; Koutras, A. A.; and Shing, P. B., "Evaluation of Collapse Resistance of Reinforced Masonry Wall Systems by Shake-Table Tests," *Earthquake Engineering & Structural Dynamics*, V. 50, No. 2, 2021, pp. 475-494. doi: 10.1002/eqe.3342